Journal of Nanobiotechnology

RESEARCH

Open Access

Amelioration of the rheumatoid arthritis microenvironment using celastrol-loaded silver-modified ceria nanoparticles for enhanced treatment

Xiaoru Zhang[1†], Xiaguo Fu[1†], Wanying Chen[1], Peng Chen[3], He Zhu[3], Bo Yang[2*], Jianming Liang[1*] and Feng Zeng[1*]

Abstract

Rheumatoid arthritis (RA) is characterized by elevated levels of reactive oxygen species (ROS) and a persistent inflammatory microenvironment dominated by M1 macrophages, both of which contribute to disease progression. To address these pathological features, we developed a core–shell nanoplatform consisting of silver-modified ceria nanoparticles loaded with celastrol (Ag-CeNP@Cel). This nanoplatform significantly enhances the water solubility of celastrol and reduces its hepato-renal toxicity by enabling passive accumulation in inflamed joints. The silver-modified ceria nanoparticles synergistically combine with celastrol to scavenge excess ROS and reprogram M1 macrophages into M2 macrophages, thereby mitigating inflammatory responses and improving the rheumatoid arthritis microenvironment (RAM). Ag-CeNP@Cel exhibited robust therapeutic efficacy and safety in preclinical models, presenting an innovative approach to RA treatment by integrating ROS elimination with macrophage modulation to ameliorate inflammatory microenvironment. This study underscores the potential of Ag-CeNP@Cel as a promising therapeutic strategy for RA management.

Keywords Nanoplatform, Rheumatoid arthritis, Rheumatoid microenvironment, Reactive oxygen species, Macrophages

[†]Xiaoru Zhang and Xiaguo Fu have contributed equally to this work.

*Correspondence:
Bo Yang
15521116357@163.com
Jianming Liang
liangjianming@gzucm.edu.cn
Feng Zeng
zengfeng@gzucm.edu.cn
Full list of author information is available at the end of the article

Graphical Abstract

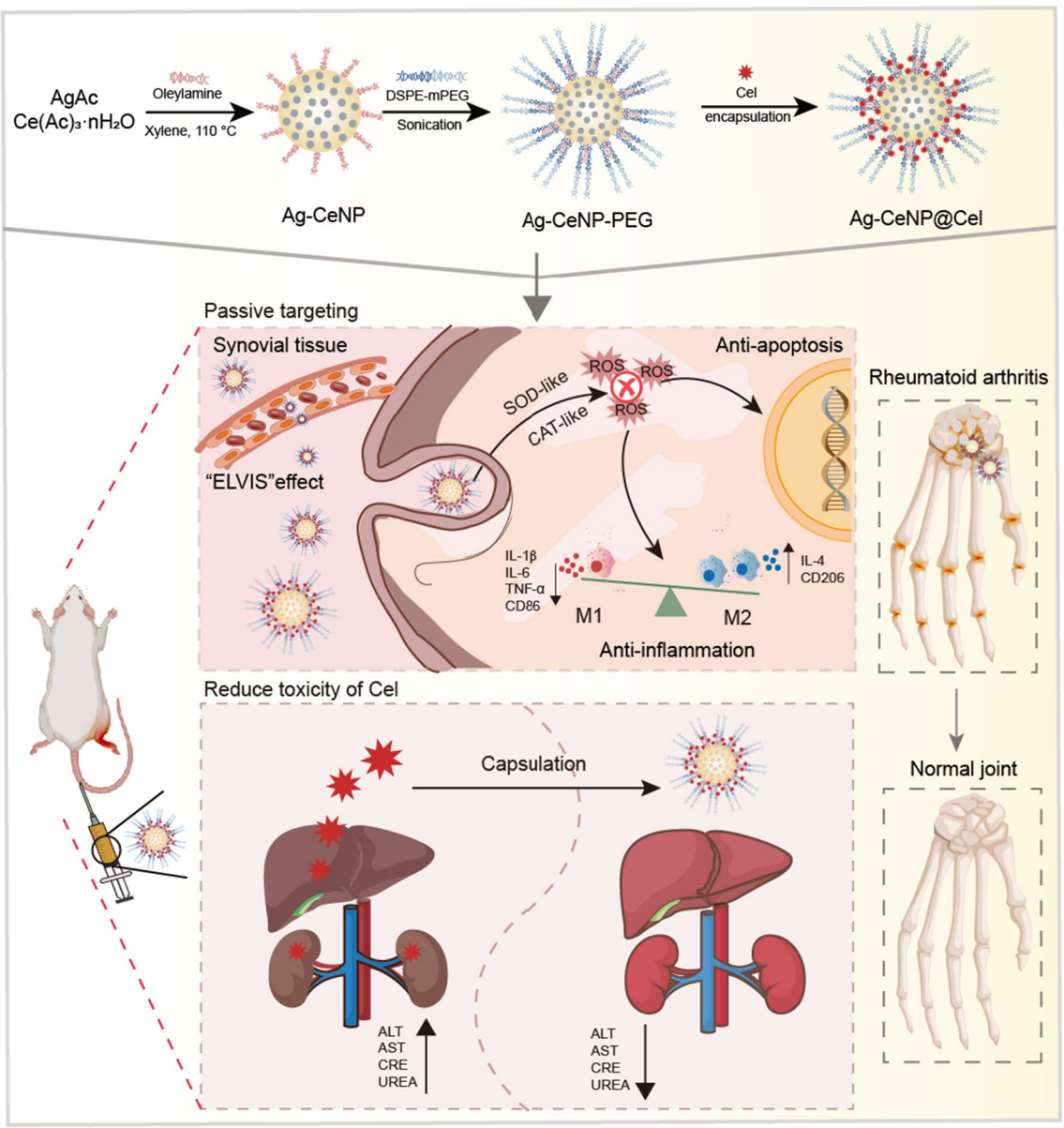

Introduction

Rheumatoid arthritis (RA) is a chronic autoimmune disorder characterized by persistent inflammation, synovitis, and progressive joint damage that can significantly impair quality of life and lead to disability [1]. Beyond joint complications, RA is associated with a range of systemic comorbidities, including skeletal disease, pulmonary complications, cardiovascular issues, and psychological impact [2]. Current treatment options, such as non-steroidal anti-inflammatory drugs (NSAIDs), glucocorticoids (GCs), and disease-modifying antirheumatic drugs (DMARDs), offer symptomatic relief and moderate disease control. However, achieving sustained remission remains difficult due to limited efficacy over time and the risk of adverse effects from prolonged use, including interstitial lung disease, bone marrow dysfunction, hyperglycemia, and liver toxicity [3, 4]. Although biological agents, including

cytokine-targeting antibodies like infliximab and tocilizumab, have shown efficacy in RA management, they come with challenges such as high costs, systemic immunosuppression, and adverse effects like tuberculosis reactivation [5–7]. Importantly, some patients experience inadequate responses or diminishing efficacy with biologic therapies, highlighting the need for more effective and safer treatment strategies [7].

The pathophysiology of RA is largely driven by high levels of reactive oxygen species (ROS) and pro-inflammatory cytokines, which contribute to a sustained inflammatory environment known as the RA microenvironment (RAM) [2, 8, 9]. Macrophages play a central role in RA, and their polarization status critically influences the inflammatory dynamics within the joint [10]. Macrophage polarization can be broadly divided into the proinflammatory classically activated (M1) phenotype and anti-inflammatory alternatively activated (M2) phenotype [11]. In RA, proinflammatory M1 macrophages dominate, perpetuating inflammation through the secretion of cytokines such as IL-1β, IL-6, and TNF-α. Alternatively, M2 macrophages, which have anti-inflammatory properties and secrete cytokines like IL-4, IL-10, and TGF-β, are present at lower levels in RA [12, 13]. Elevated ROS levels in the RAM further exacerbate inflammation by promoting M1 macrophage polarization and hindering M2 polarization. Thus, targeting ROS to shift macrophage polarization from M1 to M2 represents a promising strategy for alleviating inflammation and modulating the inflammatory environment in RA [2, 9, 13–15].

Celastrol (Cel), a bioactive compound from *Tripterygium wilfordii* Hook F, has shown potential in RA treatment due to its ability to modulate macrophage polarization and protect the inflamed joint environment [16, 17]. However, its clinical application is limited by poor water solubility, a narrow therapeutic window, and severe organ toxicity [18, 19]. Recent research suggests that catalytic metallic nanoparticles, known for their excellent ROS-scavenging properties, may be viable alternative for RA treatment [4, 13, 15]. Silver nanoparticles (AgNPs), for instance, have demonstrated potent antioxidative and anti-inflammatory effects by reducing ROS levels and promoting the M1-to-M2 macrophage shit [4]. However, AgNPs are prone to degradation under high temperatures and ionic strength conditions, which limits their stability and efficacy [20]. AgNPs can be stabilized by incorporating reducible ceria nanoparticles (CeNP) support structures [21]. CeNP are robust antioxidants and anti-inflammatory agents that can effectively scavenge multiple ROS and reduce proinflammatory cytokine levels. Doping CeNP with silver enhances the valence state transition between Ce^{3+} and Ce^{4+}, thereby improving their ROS scavenging capacity [22]. Our previous research has shown that CeNP provides neuroprotective and anti-inflammatory effects by modulating inflammatory microenvironments [23, 24].

In this study, a novel silver-modified ceria nanoparticle (Ag-CeNP) with a core–shell structure was developed. The core consists of monodispersed ultrasmall Ag-CeNP, while the shell is made of organic DSPE-$mPEG_{2k}$, which also encapsulates Cel. The Ag-CeNP@Cel nanoplatform has the ability to effectively accumulate in inflamed lesions through the "ELVIS" effect (Extravasation through Leaky Vasculature and subsequent Inflammatory cell-mediated Sequestration). The combination of ROS-scavenging Ag-CeNP-PEG with Cel provides synergistic anxi-oxidiant and anti-inflammatory actions, offering the potential to lower Cel dosages, minimize toxicity, and improve therapeutic efficacy in RA (Scheme 1). This strategy provides a promising framework for enhancing the safety and effectiveness of RA treatments by integrating ROS reduction with targeted macrophage modulation.

Results

Synthesis and characterization of Ag-CeNP and Ag-CeNP@Cel

We synthesized Ag-CeNP@Cel according to the following steps (Fig. 1A). First, the hydrophobic uniform-size ultrasmall nanozyme core Ag-CeNP was constructed by a modified sol–gel reaction [22, 24]. Subsequently, owing to the strong ligand binding between oleylamine on the surface of the nanozyme core and the phospholipid of DSPE-$mPEG_{2k}$, the hydrophobic Ag-CeNP were transferred from organic phase into the hydrophilic phase after encapsulated with phase transfer agent DSPE-$mPEG_{2k}$ [25]. The PEGylation improves water-dispersity, and biocompatibility and extends the half-lives in the bloodstream of nanozyme [26]. Finally, the anti-RA molecular Cel was loaded in the organic shell on the Ag-CeNP-PEG by van der Waals forces and organic macromolecules absorption [27]. The hydrodynamic diameter of Ag-CeNP-PEG based on dynamic light scattering (DLS) measurements was 6.77 ± 1.60 nm with a polydispersity index (PDI) of 0.37 ± 0.10 (Fig. 1B, Figure S1A), and the *zeta* potential was -0.01 ± 0.13 mV (Fig. 1C). After loaded Cel, the entrapment efficiency (*EE*%) of Cel was 87.07% and the hydrodynamic diameter of Ag-CeNP@Cel was increased to 8.53 ± 0.26 nm with a PDI of 0.24 ± 0.05 (Fig. 1D, Figure S1B), and the *zeta* potential was changed to -8.94 ± 0.73 mV (Fig. 1E). The changes in hydrodynamic diameter and *zeta* potential confirmed the successful loading of Cel in the organic shell of Ag-CeNP. The hydrodynamic diameter and relative turbidity of Ag-CeNP-PEG and Ag-CeNP@Cel did

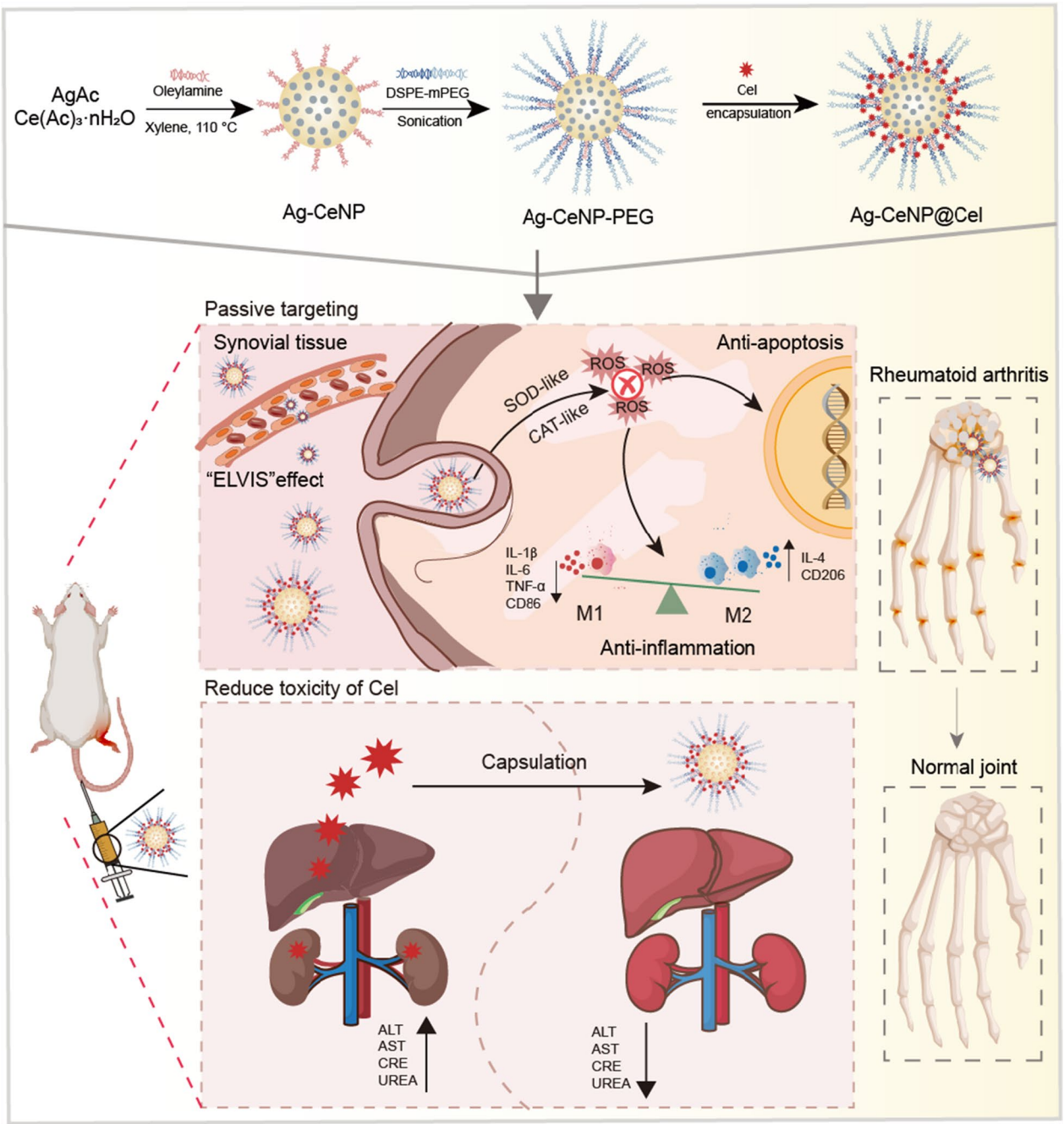

Scheme 1. Therapeutic mechanisms of Ag-CeNP@Cel in rheumatoid arthritis treatment. The Ag-CeNP@Cel passively accumulates in inflamed joints through the "ELVIS" effect. This targeted accumulation enables effective elimination of excessive ROS, regulates macrophage polarization from pro-inflammatory M1 to anti-inflammatory M2 phenotypes, and protects vascular endothelial cells from apoptosis—thereby exerting therapeutic effects in rheumatoid arthritis. Encapsulation of Cel within the nanozyme enhances its water solubility and mitigates hepato- and nephrotoxicity, contributing to improved safety and efficacy in RA treatment

not show significant changes within 7 days, exhibiting that they do not agglomerate and have good colloidal stability in serum-containing media for over one week (Figure S2). As shown in Fig. 1F–G, the TEM images confirm that Ag-CeNP and Ag-CeNP-PEG maintain a highly facetted, crystalline spherical morphology with an ultrasmall core size of approximately 2.0 nm, which enhances catalytic efficiency and biological penetration.

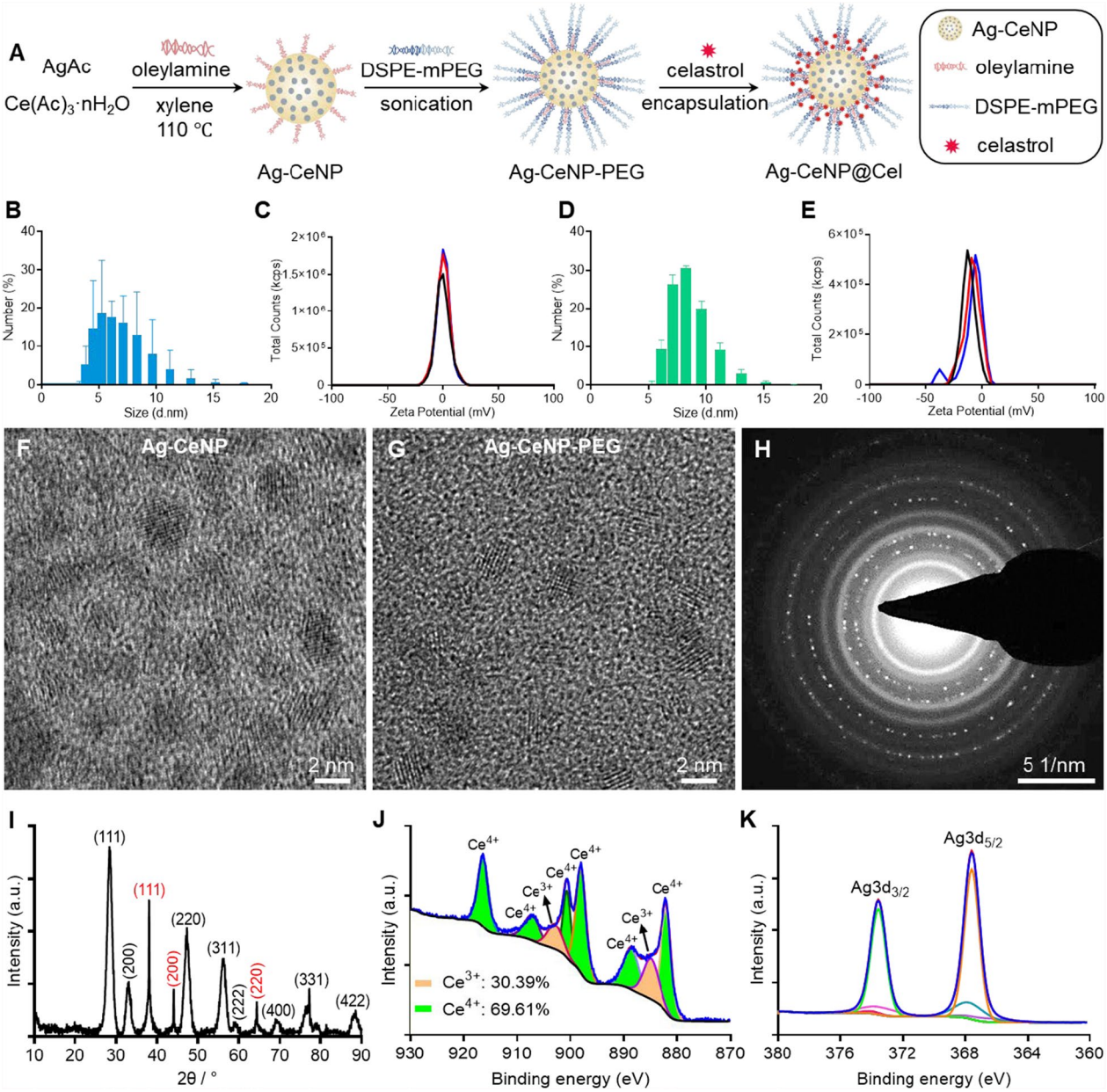

Fig. 1 Synthesis and characterization of silver-decorated ceria nanoparticle. **A** Schematic illustration of the synthetic process for Ag-CeNP, Ag-CeNP-PEG and Ag-CeNP@Cel. **B** Hydrodynamic size distribution of Ag-CeNP-PEG, determined by dynamic light scattering (DLS) in ddH_2O (n = 3). **C** Apparent *zeta* potential distribution of Ag-CeNP-PEG in ddH_2O (n = 3). **D** Hydrodynamic size distribution of Ag-CeNP@Cel, determined by DLS in ddH_2O (n = 3). **E** Apparent *zeta* potential distribution of Ag-CeNP@Cel in ddH_2O (n = 3). Representative high-resolution TEM image of hydrophobic nanozyme Ag-CeNP (**F**) and hydrophilic nanozyme Ag-CeNP-PEG (**G**). **H** The distinct lattice fringes in SAED patterns confirm the crystalline character of Ag-CeNP. **I** XRD patterns of Ag-CeNP indicate major peaks belonging to cubic phase CeNP (ICSD 55284) and minor peaks belonging to silver element (ICSD 44387). **J** Deconvoluted XPS spectrum of cerium Ce3d revealing the valence state and the corresponding binding energy peaks of Ce (III) (884.9 and 902.8 eV) and Ce (IV) (882.1, 888.6, 898.0, 900.6, 907.2 and 916.4 eV). **K** Deconvoluted XPS spectrum of silver Ag3d indicating Ag remaining in a metallic (Ag^0) state. a.u., arbitrary units

Energy-dispersive spectroscopy (EDS) verified the successful synthesis of Ag-CeNP, indicated by the necessary elements peak Ce, Ag, and O elements (Cu and C come from the carbon film) (Figure S3). Selected-area electron diffraction (SAED) patterns of Ag-CeNP showed halo-like patterns, the distinguish fringes confirmed the nanocrystalline nature (Fig. H). In addition, Fig. 1I showed the XRD patterns of Ag-CeNP, the diffraction

peaks at 2θ of 28.4°, 33.0°, 47.4°, 56.3°, 59.1°, 68.9°, 77.3° and 88.6° can be assigned to the (111), (200), (220), (311), (222), (400), (331) and (422) lattice planes of the cubic fluorite structure of ceria nanoparticles (JCPDS file NO. 34–0394), while sharp reflections of 38.0°, 44.1°, and 64.4° can be attributed to (111), (200) and (220) lattice planes of the crystalline Ag peaks, which were well matched with cubic structure of Ag (JCPDS file NO. 87–0717) [28, 29]. The XPS survey spectrum indicated Ag-CeNP was composed of Ce (880–920 eV), O (~530 eV) and Ag (~360 eV) (Figure S4). High-resolution spectra of Ce3d and Ag3d were acquired to highlight nanozyme surface chemical character. The Ce3d envelope revealed characteristic mixed valence state of Ce^{3+} (884.9 and 902.8 eV) and Ce^{4+} (882.1,888.6, 898.0, 900.6, 907.2 and 916.4 eV) (Fig. 1J), this result is consistent with our previous research [23, 24]. Ag3d spectra consist of spin–orbit coupling $Ag3d_{3/2}$ and $Ag3d_{5/2}$ whose binding energies were 368.1 eV and 374.1 eV, respectively (Fig. 1K), which were excellent agreement with the reported AgNPs [30, 31].

Antioxidative activity of Ag-CeNP@Cel

To demonstrate the superiority of Ag-CeNP-PEG, we compared its ROS scavenging activity and macrophage polarization regulation with CeNP-PEG. The results showed that Ag-CeNP-PEG exhibited significantly higher DPPH free radical scavenging activity (Figure S5A), as well as enhanced superoxide dismutase (SOD)-like (Figure S5B) and peroxidase (POD)-like (Figure S5C) activities, compared to CeNP-PEG. In contrast, its hydroxyl radicals (•OH) scavenging activity (Figure S5D) and catalase (CAT)-like decomposition of hydrogen peroxide (H_2O_2) into O_2 (Figure S5E) were comparable to those of CeNP-PEG. Cell-based experiments further confirmed that Ag-CeNP-PEG was more effective than CeNP-PEG in reducing intracellular ROS levels (Figure S6). Additionally, although both CeNP-PEG and Ag-CeNP-PEG reduced the M1-type polarization of BMDM, Ag-CeNP-PEG exhibited a stronger effect (Figure S7).

The hydroxyl radical antioxidant capacity (HORAC), SOD, and CAT of nanozyme were investigated by electron paramagnetic resonance (EPR) spectroscopy. EPR spectra showed the concentration-dependent scavenging activity of Ag-CeNP-PEG against •OH, superoxide anions ($O_2^{\bullet-}$), and H_2O_2. As the concentration of Ag-CeNP-PEG increased, its capacity to neutralize •OH was enhanced (Fig. 2A), with a similar trend observed for $O_2^{\bullet-}$ scavenging (Fig. 2B). In Fig. 2C, the concentration-dependent reduction in H_2O_2 further confirmed the CAT-mimetic activity of Ag-CeNP-PEG. Next, the radical scavenging activity of Ag-CeNP@Cel was also evaluated by the Superoxide Dismutase Assay Kit and Catalase Assay Kit. The results indicated that at the same nanozyme concentration, the SOD activity (units/μg) of Ag-CeNP@Cel was 0.4 times higher than Ag-CeNP-PEG. Additionally, at the same Cel concentration, the SOD activities (units/μg) of Ag-CeNP@Cel were 2.8 times higher than those of free Cel (Fig. 2D). Furthermore, at the same concentration, the CAT activity (units/μg) of Ag-CeNP@Cel was 0.2 times higher than that of Ag-CeNP-PEG and 0.7 times higher than that of free Cel (Fig. 2E). In addition, as shown in Figure S8, the reactive nitrogen species (RNS) elimination activity of Ag-CeNP@Cel was more pronounced than that of Ag-CeNP-PEG at the same nanozyme concentration and incubation time. The in vitro antioxidant activity of Ag-CeNP@Cel was further demonstrated using fluorescence microscopy and flow cytometry, employing the ROS probe Dihydrorhodamine 123 (DHR123). Flow cytometry analysis revealed that after 24 h of incubation with H_2O_2 (1.0 mmol/L), the ROS level in human umbilical endothelial cells (HUVEC) increased by 8.1 times. However, co-incubation with free Cel, Ag-CeNP-PEG, and Ag-CeNP@Cel significantly reduced by 77.7%, 84.2%, and 88.3%, respectively (Fig. 2F). The above results were validated by fluorescence microscopy, and intracellular ROS levels were significantly reduced after treatment with free Cel, Ag-CeNP-PEG, and Ag-CeNP@Cel (Fig. 2G), indicating that Ag-CeNP@Cel can alleviate oxidative stress induced by H_2O_2.

The cytotoxicity, uptake, and effects of Ag-CeNP@Cel on macrophage phenotype transitions

To test in vitro biocompatibility, the cytotoxicity of free Cel, Ag-CeNP-PEG, and Ag-CeNP@Cel was assessed on bone marrow-derived macrophages (BMDM) and HUVEC via MTT assay. After 24 h treatment, free Cel showed obvious cytotoxicity to BMDM at concentration higher than 0.16 μg/mL (Fig. 3A), and Ag-CeNP-PEG did not show cytotoxicity within a Ce concentration of 2 μg/mL (Fig. 3B), the cytotoxicity of Ag-CeNP@Cel was lower than that of free Cel (Fig. 3C), suggesting that loading Cel to Ag-CeNP-PEG reduced its cytotoxicity. The cytotoxicity of free Cel, Ag-CeNP-PEG, and Ag-CeNP@Cel against HUVEC exhibited a comparable pattern (Figure S9). As illustrated in Figure S10A, approximately 50% of the cells succumbed after incubation with 1 mmol/L H_2O_2 for 24 h. Thus, this concentration was selected for modeling oxidative damage cell models. The free Cel, Ag-CeNP-PEG, and Ag-CeNP@Cel were observed to enhance the viability of H_2O_2-stimulated HUVEC, with the Ag-CeNP@Cel demonstrating the most pronounced effect (Figure S10B). To further study the anti-apoptotic effect of Ag-CeNP@Cel, apoptotic cells were quantified using the Annexin V-FITC/PI assay. Total apoptotic

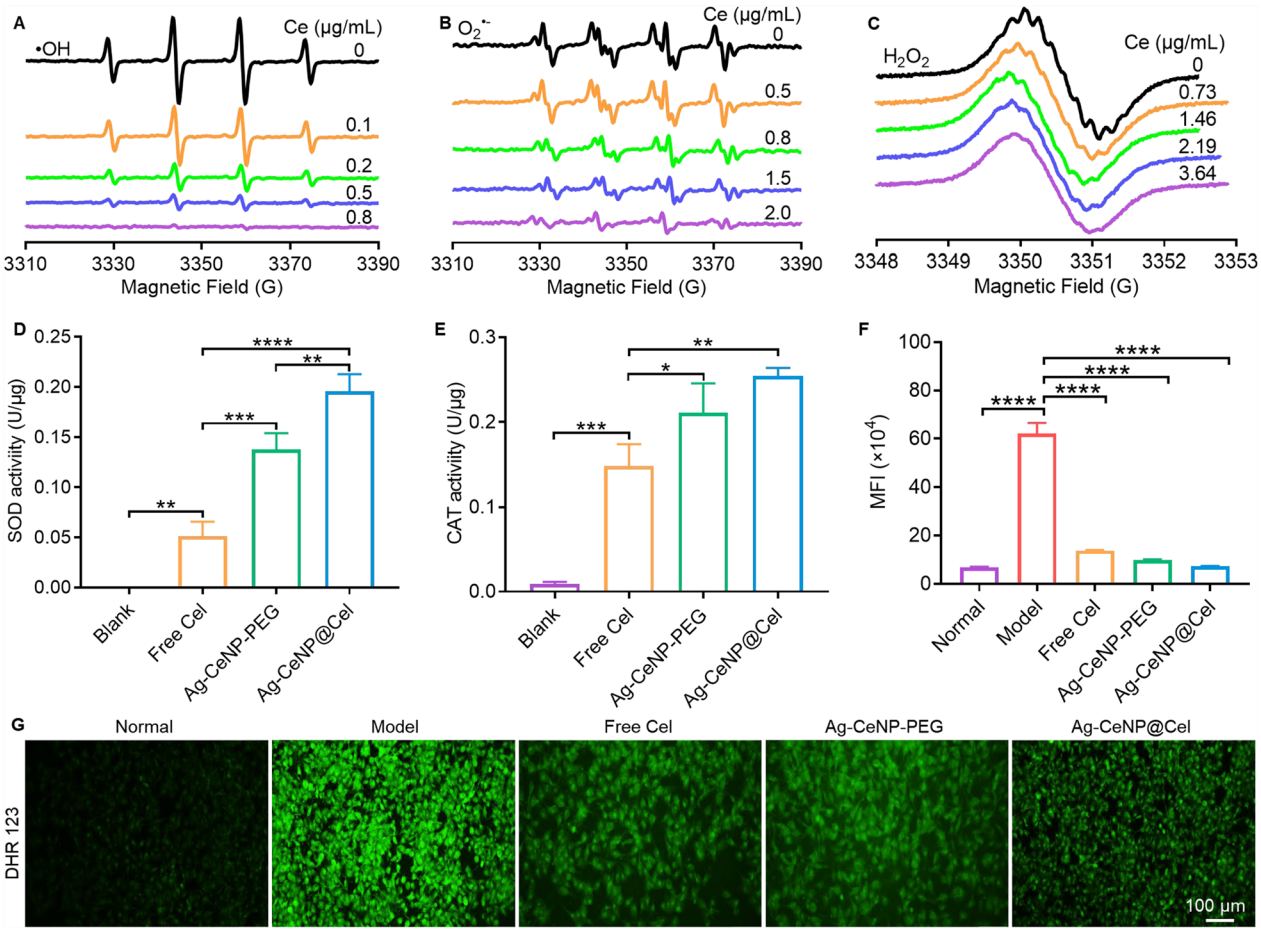

Fig. 2 In vitro ROS scavenging activities of Ag-CeNP@Cel. EPR spectra demonstrated concentration-dependent scavenging activities of Ag-CeNP-PEG to •OH (**A**), $O_2^{\bullet-}$ (**B**), and H_2O_2 (**C**). **D** SOD-like activity of Ag-CeNP@Cel assessment by SOD activity assay kit (n = 3). **E** The catalase-like activity of Ag-CeNP@Cel assessment by CAT activity assay kit (n = 3). **F** Flow cytometric analysis evaluating the ROS levels in HUVEC after different treatments (n = 3). **G** Representative fluorescence microscopy images of HUVEC with different treatments and stained with ROS fluorescent probe DHR 123. Scar bar = 100 μm. The data are shown as the mean ± SD. One-way ANOVA was used for statistical analysis. (**$p < 0.01$, ***$p < 0.001$, ****$p < 0.0001$)

cells were 19.19 ± 0.95% in the H_2O_2-stimulated model group, it decreased to 16.29 ± 0.22%, 13.53 ± 0.25%, and 12.88 ± 0.18% after treatment with free Cel, Ag-CeNP-PEG, and Ag-CeNP@Cel, which indicated that the anti-apoptosis effect of Ag-CeNP@Cel more significant than free Cel and Ag-CeNP-PEG on H_2O_2-stimulated cells model (Fig. 3D-E). The cellular uptake of nanozyme was explored by monitoring the Ag-CeNP-PEG labeled with Nile Red. Normal and injured HUVEC were used as models. Flow cytometry revealed that cellular uptake was as early as 30 min after the addition of Ag-CeNP-PEG and internalized by cells in a time-dependent manner. Moreover, the nanoparticle uptake efficiency of H_2O_2-injured HUVEC was higher than that of normal HUVEC (Fig. 3F), indicating that nanozyme was more likely to enter cells damaged by oxidative stress to exert protective effects. BMDM was used to determine the capability of Ag-CeNP@Cel for reprogramming macrophages (Fig. 3G). Flow cytometry showed that CD86, a marker of pro-inflammatory macrophages, was pronounced in LPS + IFN-γ stimulated BMDM, while treatment with free Cel, Ag-CeNP-PEG, and Ag-CeNP@Cel decreased CD86 expression by 25.0%, 74.3% and 80.8%, respectively (Figure S11, Fig. 3H). Interestingly, the expression of the anti-inflammatory macrophage marker CD206, was decreased in LPS + IFN-γ stimulated BMDM, after free Cel, Ag-CeNP-PEG, and Ag-CeNP@Cel treatment, increased by 25.6%, 57.5%, and 103.2%, respectively (Figure S12, Fig. 3I). The ratio of CD86/CD206 was markedly diminished by treatment with free Cel, Ag-CeNP-PEG, and Ag-CeNP@Cel, with Ag-CeNP@Cel exhibiting the most pronounced effect (Fig. 3J). Collectively, these results suggested that Ag-CeNP@Cel effectively repolarizes pro-inflammatory

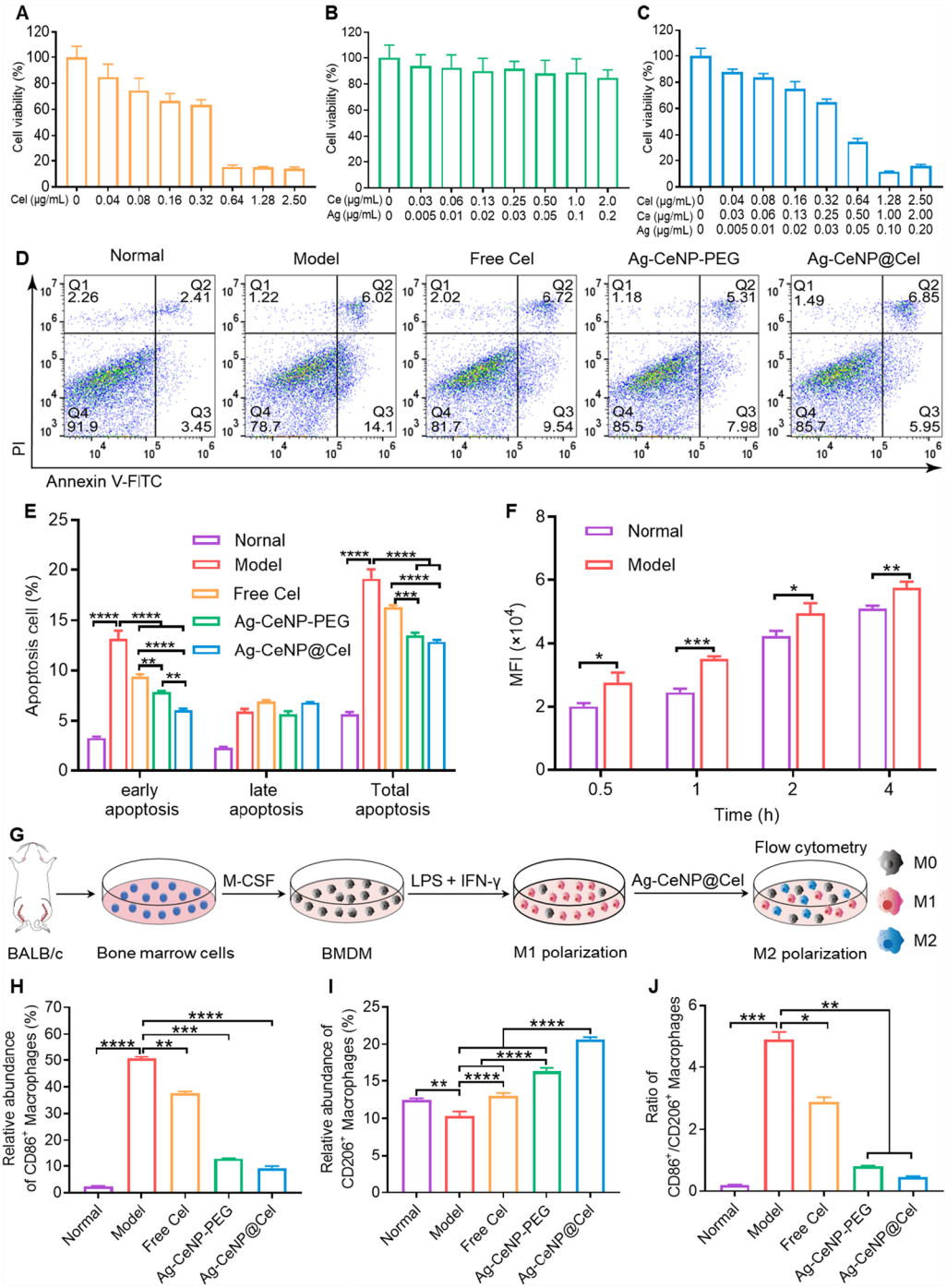

Fig. 3 In vitro cytotoxicity, uptake, and macrophage phenotype transition test of Ag-CeNP@Cel. The viability of BMDM post-treatment of free Cel (**A**), Ag-CeNP-PEG (**B**), and Ag-CeNP@Cel (**C**) for 24 h (n = 6). **D** Flow cytometry based on Annexin V-FITC/PI apoptosis detection kit post-stimulated by 1 mM H_2O_2 and then treatment of free Cel, Ag-CeNP-PEG, or Ag-CeNP@Cel for 24 h. **E** The quantification of apoptosis of HUVEC post varied treatment (n = 3). **F** Quantitative analysis of the in vitro cellular uptake of Nile Red-labelled Ag-CeNP-PEG in normal HUVEC and H_2O_2 stimulated HUVEC detected by flow cytometry (n = 3). **G** Schematic diagram of the experimental setup to investigate the effect of Ag-CeNP@Cel modulate the phenotype of macrophage. Quantitative analysis of M1 macrophage markers CD86 (**H**) and M2 macrophage marker CD206 (**I**) by flow cytometry treated with various treatments (n = 3). **J** The ratio of M1 and M2 macrophages in different treatment groups (n = 3). The data are shown as the mean ± SD. One-way ANOVA was used for statistical analysis. (*$p < 0.05$, **$p < 0.01$, ***$p < 0.001$, ****$p < 0.0001$)

macrophages to anti-inflammatory macrophages, thereby exerting an anti-inflammatory effect.

In vivo targetability of Ag-CeNP-PEG

The in vivo targetability of Ag-CeNP-PEG was investigated using adjuvant-induced arthritis (AIA) murine model, which was developed through intradermal injection of complete Freund's adjuvant into the right hind paws [32]. This model mimics key pathological features of human RA, including chronic inflammation, cartilage degradation, and bone destruction. To assess the accumulation of Ag-CeNP@Cel in inflamed joints, Did-labeled Ag-CeNP-PEG and free Ag-CeNP-PEG were administered intravenously to both normal and AIA mice. The distribution was tracked using an optical imaging system and quantified by inductively coupled plasma mass spectrometer (ICP-MS). As shown in Fig. 4A, no significant fluorescence was detected in the paws of normal mice during the 24 h observation period. However, the inflamed paws of AIA model mice exhibited much stronger fluorescence signals compared to the contralateral non-inflamed paws and the paws of normal mice. Notably, the fluorescence intensity in the inflamed paws increased gradually over time, peaking at 8 h post-injection and remaining strong for at least 24 h. Ex vivo imaging of the joints at 24 h post-injection further confirmed these results. While no fluorescence was detected in the non-inflamed legs of normal mice, the inflamed legs of AIA mice displayed strong fluorescence (Fig. 4B). Semi-quantitative analysis of fluorescence intensity revealed that the inflamed legs of AIA mice had approximately fourfold higher fluorescence compared to the non-inflamed legs of normal mice (Figure S13). Ex vivo imaging of organs revealed that a significant number of Ag-CeNP-PEG nanoparticles accumulated in the liver and spleen (Fig. 4C, D), likely due to capture by the reticuloendothelial system (RES). Additionally, a smaller amount of nanoparticles was detected in the lungs (Fig. 4C, D). Consistent with the optical imaging results, quantitative data from ICP-MS demonstrated that the Ce concentration in inflamed joints was 0.30 ± 0.04 μg/g, which is three times higher than in normal joints (0.10 ± 0.02 μg/g) (Fig. 4E). After intravenous injection, the majority of nanoparticles were sequestered by the RES, primarily accumulating in the liver and spleen (Fig. 4F). These findings highlight the in vivo targeting ability of Ag-CeNP@Cel, demonstrating its selective accumulation in inflamed joints. This passive accumulation of nanoparticles in inflamed areas can be attributed to the "ELVIS" effect, as previously established in related studies [4, 33].

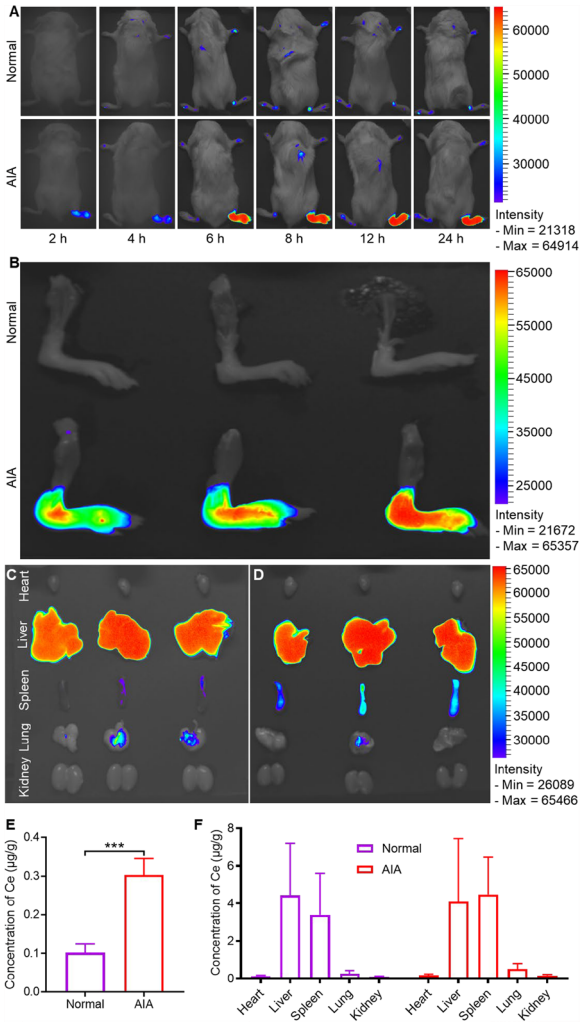

Fig. 4 High arthritis-targeting efficiency of Ag-CeNP-PEG. **A** Real-time near-infrared fluorescence imaging of Did-labelled Ag-CeNP-PEG at selected time points post intravenous injection in normal and AIA mice. **B** Ex vivo fluorescent imaging of Did-labelled Ag-CeNP-PEG in hind limbs of normal and AIA mice 24 h post-injection of Ag-CeNP-PEG. Ex vivo fluorescent imaging of Did-labelled Ag-CeNP-PEG in heart, liver, spleen, lung, and kidney of normal (**C**) and AIA mice (**D**) at 24 h post-injection. **E** ICP-MS analysis of Ag-CeNP-PEG accumulation in normal and RA-affected joints (n = 4). **F** ICP-MS analysis of Ag-CeNP-PEG distribution in the heart, liver, spleen, lungs, and kidneys of normal and RA mice (n = 4). The data are shown as the mean ± SD. One-way ANOVA was used for statistical analysis. (***$p < 0.001$)

In vivo therapeutic efficacy of Ag-CeNP@Cel on AIA mice

The in vivo therapeutic efficacy of Ag-CeNP@Cel was evaluated in AIA mice. Figure 5A illustrates the temporal progression of the RA model establishment and treatment. At the end of the therapeutic process, the mean body weights of the model group, the Ag-CeNP-PEG group, the free Cel group, and the Ag-CeNP@Cel group

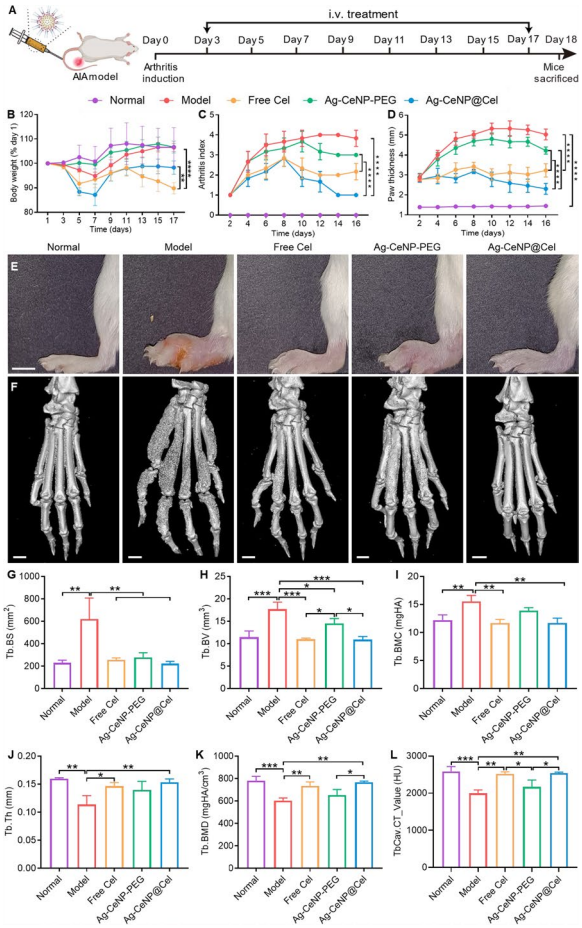

Fig. 5 In vivo anti-arthritis efficacy of Ag-CeNP@Cel. **A** The schematic illustration of the experimental timeline for Ag-CeNP@Cel treatment for AIA mice. The variation of body weight percentage (**B**), arthritis index (**C**), and paw thickness (**D**) of AIA mice during the treatment period (n = 6). Representative images of right hind paws (**E**) and three-dimensional reconstruction of micro-CT of the right hind paws (**F**) at the endpoint of the experiment from each group. Quantitative bone tissue analysis parameters of Tb.BS (**G**), Tb.BV (**H**), Tb.BMC (**I**), Tb.Th (**J**), Tb.BMD (**K**) and TbCav.CT_Value (**L**), as calculated from the micro-CT scanning results (n = 4). Scale bar: 5 mm in E, and 1 mm in F. The data are shown as the mean ± SD. One-way ANOVA was used for statistical analysis. (*$p < 0.05$, **$p < 0.01$, ***$p < 0.001$, ****$p < 0.0001$)

at the end of the experiment were 106.5%, 106.7%, 89.8%, and 98.3% of their respective baseline weights, respectively. These findings suggest that free Cel may possess a higher degree of toxicity, whereas the encapsulation of Cel within nanozyme may have effectively mitigated its toxicity (Fig. 5B). While Ag-CeNP-PEG was ineffective in reducing the arthritis index and paw thickness in AIA mice, free Cel showed some therapeutic effects. In contrast, Ag-CeNP@Cel significantly reduced the arthritis index and alleviated ankle joint swelling compared to both free Cel and Ag-CeNP-PEG (Fig. 5C, D). As shown in Fig. 5E, compared to healthy mice, mice in the model group experienced severe joint swelling, while mice treated with free Cel and Ag-CeNP-PEG showed moderate improvement, with reduced swelling. The Ag-CeNP@Cel group, however, displayed significant reductions in joint swelling. Micro-CT scans confirmed these findings, with severe bone erosion in the model group and some reduction in bone damage in the free Cel and Ag-CeNP-PEG groups. Notably, the Ag-CeNP@Cel group exhibited minimal bone erosion and smooth bone surfaces (Fig. 5F, Figure S14), indicating substantial improvement in the progression of bone damage. Several key histomorphometric indices based on micro-CT scans were also evaluated, including trabecular bone surface (Tb.BS), trabecular bone volume (Tb.BV), trabecular bone mineral content (Tb.BMC), trabecular thickness (Tb.Th), trabecular bone mineral density (Tb.BMD), and TbCav.CT_Value. In the AIA mouse model, Tb.BS, Tb.BV, and Tb.BMC was significantly increased, while Tb.BMD, Tb.Th and TbCav.CT_Value was decreased compared to the control group. However, treatment with free Cel, Ag-CeNP-PEG, and Ag-CeNP@Cel effectively decreased Tb.BS, Tb.BV, and Tb.BMC while increasing Tb.BMD and Tb.Th. Notably, the Ag-CeNP@Cel group recovered to levels closest to the control group (Fig. 5G-L), demonstrating its efficacy in halting and repairing bone erosion. Overall, these results suggest that Ag-CeNP@Cel can effectively terminate bone erosion progression and enhance its repair, with Cel-loaded Ag-CeNP-PEG significantly augmenting therapeutic outcomes.

Anti-inflammatory mechanism of Ag-CeNP@Cel in RA

The anti-inflammatory mechanism of Ag-CeNP@Cel in RA was investigated through a series of experiments. The relative abundance of pro-inflammatory (M1) macrophages was elevated in the inflamed joints of AIA model mice, but this was reduced following treatment with the various formulations (Figure S15, Fig. 6A), with Ag-CeNP@Cel showing the most effective shift from a pro-inflammatory (M1) to an anti-inflammatory (M2) macrophage phenotype (Figure S16, Fig. 6B). The percentage of $Foxp3^+$ $CD25^+$ regulatory T cells (Tregs), which were reduced in the AIA model group, was significantly restored with treatment, with Ag-CeNP@Cel showing a particularly strong recovery effect (Figure S17, Fig. 6C). Additionally, untreated AIA mice exhibited the highest percentage of $CD31^+$ cells, indicating the involvement of angiogenesis in RA progression and highlighting the selective accumulation of Ag-CeNP@Cel in the inflamed joint (Figure S18, Fig. 6D). Vimentin-positive synovial fibroblasts, which are responsible for synovial hyperplasia and joint destruction in RA, were

significantly increased in the AIA model group but were effectively reduced by Ag-CeNP@Cel treatment, showing the most pronounced decrease among all treatments (Figure S19, Fig. 6E). Cytokine analysis revealed that the AIA model mice had the highest concentrations of pro-inflammatory cytokines (IL-1β, IL-6, and TNF-α) and the lowest levels of anti-inflammatory cytokine (IL-4). Treatment with Ag-CeNP@Cel significantly reduced pro-inflammatory cytokines while increasing anti-inflammatory cytokine levels in both serum (Fig. 6F) and inflamed joints (Fig. 6G), confirming its ability to restore immune regulation in AIA.

Histological evaluation of inflammation and cartilage preservation in RA After Ag-CeNP@Cel treatment

To further assess the therapeutic efficacy of Ag-CeNP@Cel in reducing inflammation and preventing cartilage destruction, the right hind limbs of AIA mice were histologically analyzed at the study endpoint. Hematoxylin and eosin (H&E) staining revealed extensive inflammatory cell infiltration (red arrow area), severe synovial hyperplasia (blue arrow), and noticeable bone and cartilage destruction (green arrow) in the AIA model group compared to normal mice. While treatment with free Cel and Ag-CeNP-PEG alleviated these symptoms to some extent, Ag-CeNP@Cel significantly decreased synovial inflammation and minimized cartilage loss, bringing the condition closer to the control group (Fig. 7A). Similarly, Safranin-O staining confirmed severe cartilage degradation (orange arrows) in the AIA model group, which was partially reversed by Ag-CeNP-PEG and free Cel treatments. Ag-CeNP@Cel treatment resulted in cartilage preservation nearly identical to that in the control group (Fig. 7B). Masson staining of the joint sections showed that total collagen content (blue areas, indicated by light grey), which was greatly reduced in the AIA model group, increased after Ag-CeNP-PEG and free Cel treatments, with Ag-CeNP@Cel restoring collagen levels almost to normal (Fig. 7C). This restoration is likely related to Ag-CeNP@Cel's superior anti-inflammatory properties. Matrix metalloproteinase-3 (MMP-3) (purple arrows), a marker of synovial inflammation and joint destruction [34], was highly expressed in the AIA model group. Although free Cel and Ag-CeNP-PEG reduced MMP-3 expression slightly, Ag-CeNP@Cel significantly inhibited MMP-3, returning its levels close to those of the control group (Fig. 7D). Tissue inhibitor of metalloproteinases-1 (TIMP-1) (dark blue arrows), which protects cartilage integrity by inhibiting MMP activity, showed increased levels in the Ag-CeNP@Cel group, indicating effective control of inflammation-driven cartilage degradation (Fig. 7E). Additionally, platelet-derived growth factor A (PDGF-A) (golden arrows), a marker for tissue repair and regeneration, was elevated in the Ag-CeNP@Cel group (Fig. 7F), suggesting enhanced cartilage regeneration and joint healing. These findings highlight the superior therapeutic potential of Ag-CeNP@Cel in RA treatment by not only controlling inflammation but also promoting tissue repair and cartilage preservation.

Biosafety evaluation of Ag-CeNP@Cel in vivo

The utilization of free Cel in therapeutic regimens frequently precipitates adverse effects, treatment often results in side effects, including hepatotoxicity and nephrotoxicity, which significantly constrain its pharmacological utility [35]. Consequently, the biosafety of Ag-CeNP@Cel was assessed. The free Cel group exhibited an anomalous elevation in the liver index, whereas the Ag-CeNP@Cel group demonstrated a return to the normal range (Fig. 8A). Biochemical analysis of mouse serum revealed that treatment with free Cel resulted in a significant increase in aspartate aminotransferase (AST), alanine transaminase (ALT), creatinine (CRE), and blood urea nitrogen (UREA) concentrations. In contrast, these indicators remained within the normal range in the Ag-CeNP@Cel treatment group (Fig. 8B, C), suggesting minimal acute toxicity to the liver and kidney. H&E staining of vital organs revealed no obvious pathological changes in the heart, lung, or spleen in any of the groups. However, the free Cel group exhibited localized focal necrosis of hepatocytes accompanied by inflammatory cell infiltration, as well as degeneration of renal tubular epithelial cells (Fig. 8D). No significant abnormalities were observed in the other treatment groups (Fig. 8D). The above results suggest that free Cel has hepatotoxicity and nephrotoxicity, while loading Cel in Ag-CeNP-PEG can effectively prevent these side effects.

(See figure on next page.)

Fig. 6 Immunomodulatory, angiogenesis inhibition and anti-inflammatory effect of Ag-CeNP@Cel. Flow cytometric analysis of $CD86^+$ M1 macrophages (**A**), $CD206^+$ M2 macrophages (**B**), $Foxp3^+$ $CD25^+$ Treg cells (**C**), $CD31^+$ synovial endothelial cells (**D**) and $vimentin^+$ synovial fibroblasts (**E**) isolated from inflamed joints of AIA mice at the end point of the experiment from each group (n = 3). ELISA analyses of inflammatory cytokine (IL-1β, IL-6, and TNF-α) and anti-inflammatory cytokine (IL-4) levels in the serum (**F**) and inflamed joints (**G**) of AIA mice at the end point of the experiment from each group (n = 3). The data are shown as the mean ± SD. One-way ANOVA was used for statistical analysis. (*$p < 0.05$, **$p < 0.01$, ***$p < 0.001$, ****$p < 0.0001$)

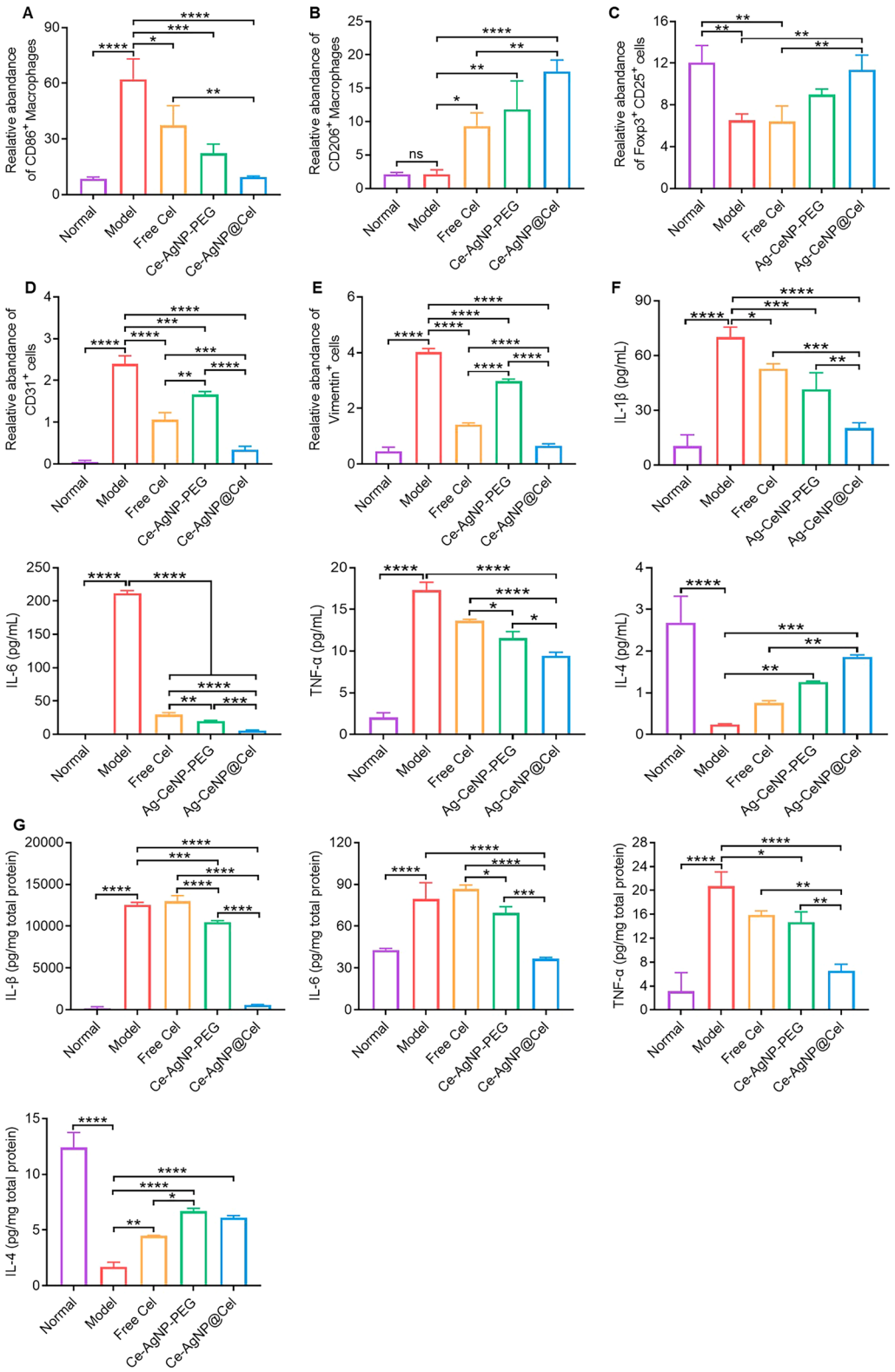

Fig. 6 (See legend on previous page.)

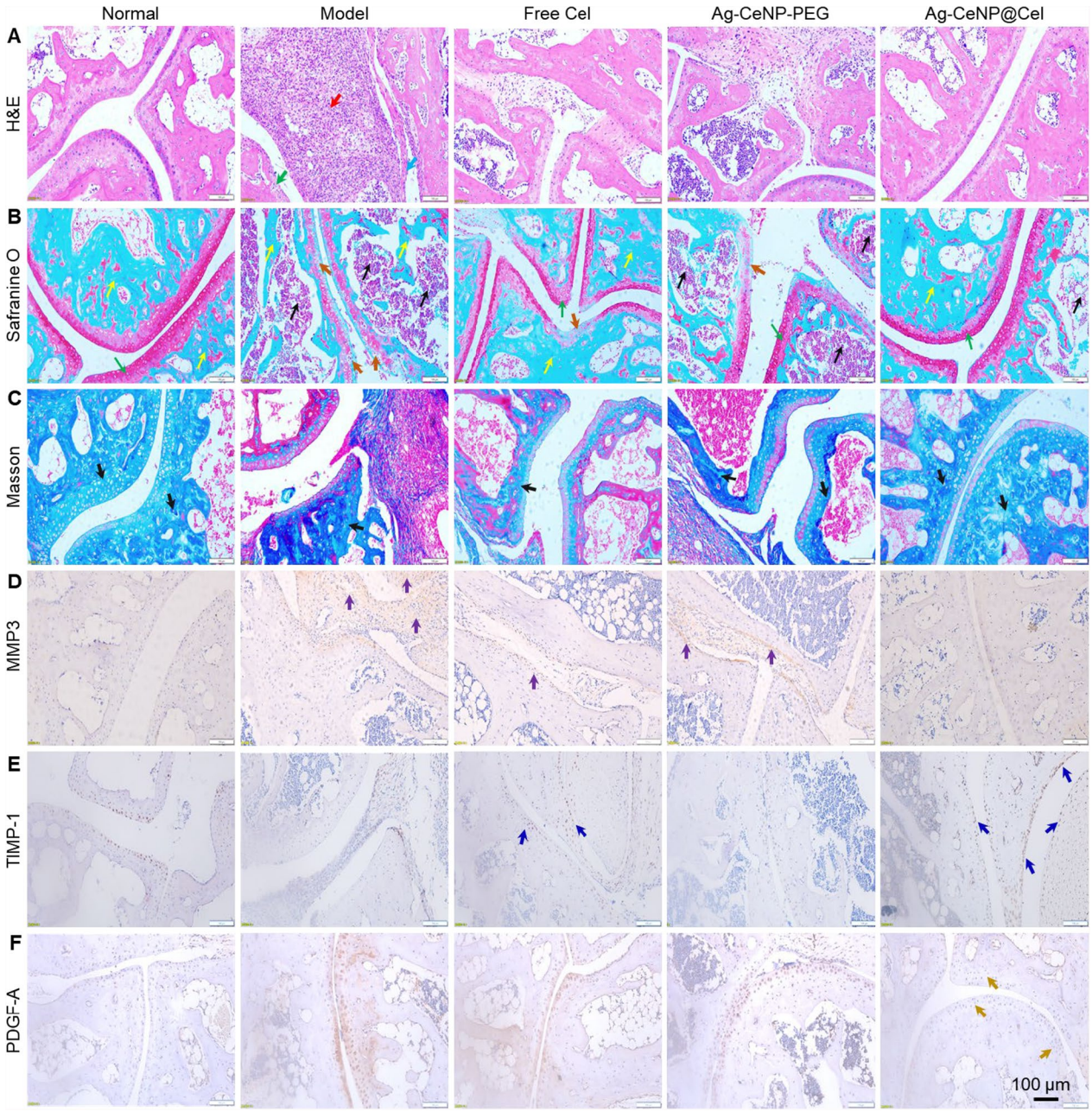

Fig. 7 Histological and immunohistochemical evaluation of the therapeutic effects of Ag-CeNP@Cel in AIA mice. Paraffin-embedded inflamed articular cartilage was stained with H&E staining (**A**), Safranine O staining (**B**) (green arrows: cartilage surface, yellow arrows: bone, black arrows: marrow cavity), and Masson staining (**C**). Representative immunohistochemistry images of the MMP3 (**D**), TIMP-1 (**E**), and PDGF-A (**F**) in the inflamed articular cartilage of AIA mice at the end point of the experiment from each group. Scale bar = 100 μm

To further assess the biosafety of Ag-CeNP@Cel, we conducted an evaluation in normal mice using a higher therapeutic dose (Cel: 6 μg/g, Ce: 1.2 μg/g, Ag: 0.23 μg/g) administered every other day for 15 days. Possibly due to the use of healthy mice, no significant weight loss was observed in any group; however, the free Cel group exhibited the slowest weight gain (Fig. 9A). Organ coefficient analysis revealed splenomegaly in the free Cel group (Fig. 9B). Moreover, AST, ALT, BUN, and CRE levels were significantly elevated in the free Cel group compared to the normal group (Fig. 9C–F), suggesting that Ag-CeNP@Cel effectively

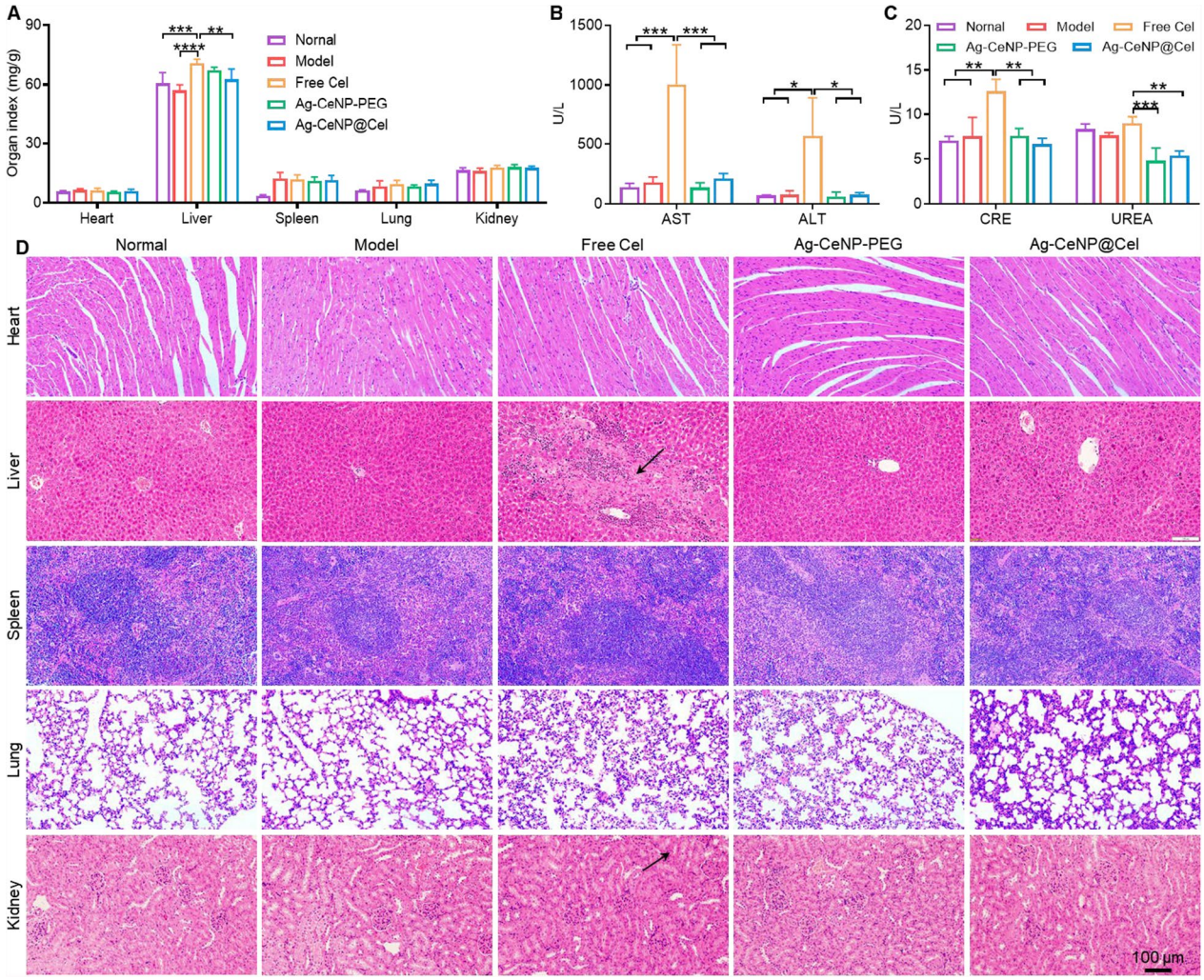

Fig. 8 Preliminary biosafety evaluation of Ag-CeNP@Cel. **A** Organ indexes of each treatment group were evaluated at the study end point (n = 6). **B** Hepatotoxicity was evaluated by measuring serum levels of AST and ALT following different treatments (n = 3). **C** Nephrotoxicity was assessed by measuring serum levels of CRE and UREA in the various treatment groups (n = 3). **D** Histological examination of major organs, including heart, liver, spleen, lung, and kidney, was performed for each group (Black arrows indicate the sites of lesions). Scale bar = 100 μm. The data are shown as the mean ± SD. One-way ANOVA was used for statistical analysis. (*$p < 0.05$, **$p < 0.01$, ***$p < 0.001$, ****$p < 0.0001$)

mitigated the hepatorenal toxicity associated with free Cel.

Discussion

RA is a disease marked by persistent inflammation, accompanied by excessive production of ROS [13]. Elevated ROS levels within the RAM drive the pro-inflammatory activation of macrophages, leading to the secretion of pro-inflammatory cytokines such as IL-1β, IL-6, and TNF-α, which subsequently regulate the recruitment, differentiation, and activation of other immune cells [2, 13, 17]. This cascade not only fuels inflammation but also contributes to cartilage and bone destruction in RA joints [36]. Celastrol is regarded as one of the top five most promising natural medicine molecules due to its potent anti-inflammatory effects [37]. It has demonstrated efficacy in the treatment of various inflammatory diseases, immune disorders, tumors, and other conditions [38]. Despite its potential, Celastrol's clinical application is limited by low bioavailability, poor water solubility, a narrow therapeutic window, and significant adverse effects, including hepatotoxicity, nephrotoxicity, and hematopoietic system toxicity [16]. To enhance its therapeutic profile, various strategies, such as developing structural derivatives, combination therapies, and nano/micro drug delivery systems, have been explored [16].

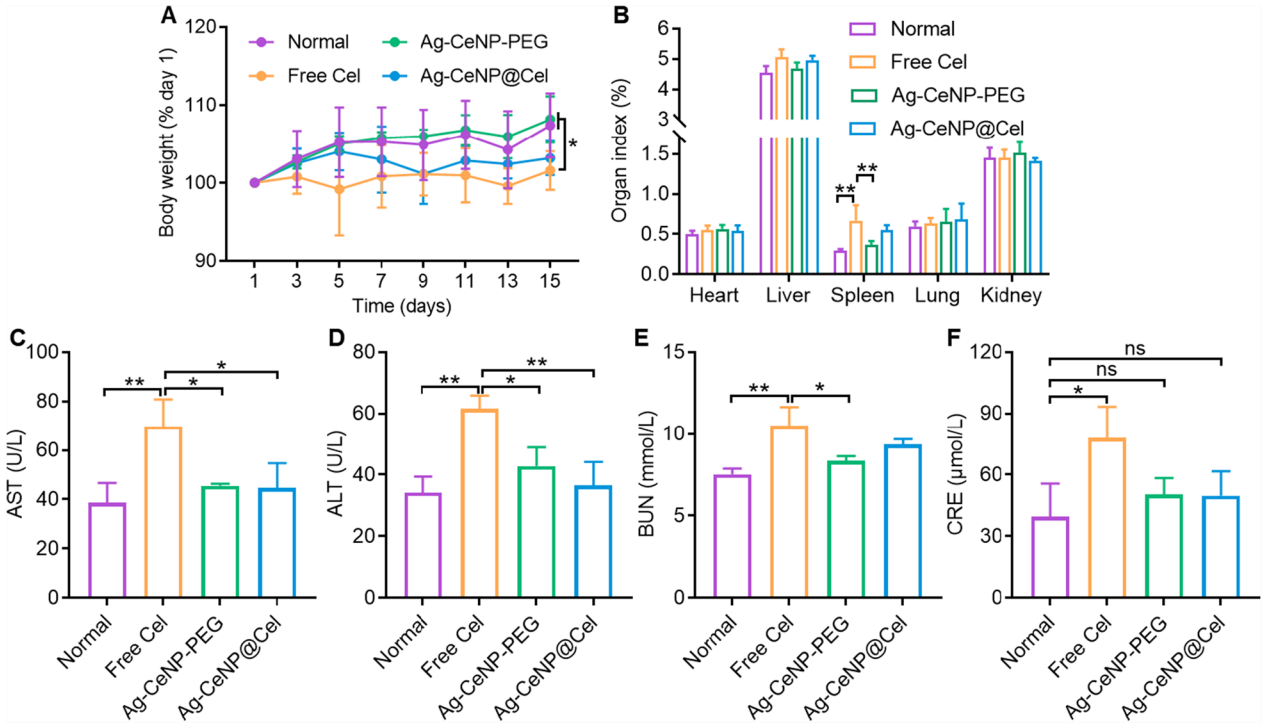

Fig. 9 Biosafety evaluation of high-dose Ag-CeNP@Cel. **A** Body weight changes in mice across different groups during the biosafety evaluation. **B** Organ index of mice in each group at the end of the experiment. Hepatotoxicity assessment based on serum AST (**C**) and ALT (**D**) levels. Nephrotoxicity assessment based on serum BUN (**E**) and CRE (**F**) levels

Emerging interest in nanocatalyst materials, particularly nanozymes with dual anti-inflammatory and antioxidant properties, has opened new possibilities for treating inflammation and ROS-related diseases, including inflammatory bowel disease (IBD), RA, stroke, and acute kidney injury (AKI) [13, 24, 27, 39]. While previous studies have explored Cel-loaded nanoparticles and AgNPs for RA [40–42], our study presents a novel dual-functional nanoplatform, Ag-CeNP@Cel, with distinct advantages. Unlike conventional Cel delivery systems that rely on Cel release for anti-inflammatory effects or AgNPs that induce M1 macrophage apoptosis through intracellular Ag^+ release—potentially causing unintended cytotoxicity—Ag-CeNP@Cel directly promotes M1-to-M2 macrophage polarization by scavenging excess ROS [4, 43]. This mechanism effectively reduces inflammation without triggering apoptosis, thereby avoiding potential toxicity. Moreover, Ag-CeNP@Cel not only serves as a Cel carrier but also harnesses the intrinsic antioxidative and anti-inflammatory properties of Ag-CeNP, creating a synergistic therapeutic effect that enhances efficacy while minimizing side effects. By integrating these advantages, our study provides a safer and more effective approach for RA treatment.

In the presented study, we developed Ag-CeNP@Cel, a nanoplatform incorporating silver-modified ceria nanoparticles (Ag-CeNP) loaded with Cel, designed to address the dual needs of reducing oxidative stress and inflammation in RA. Ag-CeNP@Cel successfully combined the antioxidant and anti-inflammatory properties of Ag-CeNP with the therapeutic effects of Cel, demonstrating efficient ROS scavenging and promoting M2 macrophage polarization. In vitro assays showed that Ag-CeNP@Cel reduced the cytotoxicity of free Cel, while in vivo, it preferentially accumulated in arthritic joints in AIA mice via the "ELVIS" effect. This targeted accumulation effectively mitigate cartilage and bone damage by modulating the RAM, balancing inflammatory cytokines, and promoting an anti-inflammatory macrophage profile. Additionally, Ag-CeNP@Cel overcomes the limitations associated with Cel's poor water solubility and systemic toxicity, positioning it as a promising candidate for RA treatment.

Conclusions

We successfully developed a nanoplatform, Ag-CeNP@Cel, an innovative nanoplatform featuring a monodispersed Ag-CeNP core, a PEG shell, and encapsulated Cel. This nanoplatform demonstrated robust ROS-scavenging activity and modulated macrophage

polarization, reducing pro-inflammatory responses and promoting anti-inflammatory effects. In vivo, Ag-CeNP@Cel effectively accumulated in arthritic joints via the "ELVIS" effect, remodeling the RAM and proving enhanced therapeutic efficacy compared to both Ag-CeNP-PEG and free Cel. Furthermore, it alleviated the hepatotoxicity and nephrotoxicity associated with free Cel, underscoring its potential to enhance both safety and effectiveness in RA therapy. These findings highlight Ag-CeNP@Cel as a promising therapeutic strategy for RA, leveraging synergistic antioxidant and anti-inflammatory mechanisms to address the challenges of current RA treatments.

Supplementary Information

The online version contains supplementary material available at https://doi.org/10.1186/s12951-025-03388-w.

Supplementary material 1.

Acknowledgements
We acknowledge the use of Grammarly and ChatGPT for helping review the writing of the manuscript to improve readability and language of the work. The authors reviewed and edited the content at the final stage and take full responsibility for the content of the publication.

Author contributions
X.Z.# and X.F.# contributed equally to this work. F.Z., J.L., and B.Y. conceived and designed the research. X.Z., X.F., and J.L. carried out the experiments and performed data analysis. W.C., H.Z., and P.C. participated in part of the experiments. F.Z. and X.Z. wrote the manuscript. F.Z., X.Z., J.L., and B.Y. revised the manuscript. All of the authors have read and approved the final manuscript.

Funding
We gratefully acknowledge the financial support by the National Natural Science Foundation of China (Nos. 32371438 to F.Z.; 82374470 to P.C.); The projects of the Department of Education of Guangdong Province (2023ZDZX2012 to F.Z.); The Special Projects in Key Areas of Colleges and Universities in Guangdong Province (2022ZDZX2015 to J.L.); The Science and Technology Program of Guangzhou (2024A04J4899 to J.L.); The Natural Science Foundation of Guangdong Province (2021A1515110727 to H.Z.); Guangzhou Science and Technology Planning Project (202201020493 to H.Z.); Young Talent Project of Guangzhou University of Chinese Medicine (A1-2601–24-414–110776 to P.C.).

Availability of data and materials
No datasets were generated or analysed during the current study.

Declarations

Ethics approval and consent to participate
All animal experiments were carried out in accordance with the approved guidelines of the Guangzhou University of Chinese Medicine Institutional Animal Care and Use Committee (pz23060).

Consent for publication
Not applicable.

Competing interests
The authors declare no competing interests.

Author details
[1]Artemisinin Research Center, Guangzhou University of Chinese Medicine, Guangzhou 510450, China. [2]Zhujiang Hospital, Southern Medical University, No.253 Industrial Avenue, Haizhu District, Guangzhou 510280, China. [3]The First Affiliated Hospital, The First Clinical Medical School, Lingnan Medical Research Center, Guangzhou University of Chinese Medicine, Guangzhou 510450, China.

Received: 7 November 2024 Accepted: 14 April 2025
Published online: 22 May 2025

References

1. Liu X, Guo R, Huo S, Chen H, Song Q, Jiang G, Yu Y, Huang J, Xie S, Gao X, Lu L. CaP-based anti-inflammatory HIF-1α siRNA-encapsulating nanoparticle for rheumatoid arthritis therapy. J Control Release. 2022;343:314–25.
2. Chen J, Zeng S, Xue Q, Hong Y, Liu L, Song L, Fang C, Zhang H, Wang B, Sedgwick AC, Zhang P, Sessler JL, Liu C, Chen J. Photoacoustic image-guided biomimetic nanoparticles targeting rheumatoid arthritis. Proc Natl Acad Sci. 2022;119(43): e2213373119.
3. Prasad P, Verma S, Surbhi GNK, Chaturvedi V, Mittal SA. Rheumatoid arthritis: advances in treatment strategies. Mol Cell Biochem. 2023;478(1):69–88.
4. Yang Y, Guo L, Wang Z, Liu P, Liu X, Ding J, Zhou W. Targeted silver nanoparticles for rheumatoid arthritis therapy via macrophage apoptosis and Re-polarization. Biomaterials. 2021;264: 120390.
5. Biesemann N, Margerie D, Asbrand C, Rehberg M, Savova V, Agueusop I, Klemmer D, Ding-Pfennigdorff D, Schwahn U, Dudek M, Heyninck K, De Tavernier E, Cornelis S, Kohlmann M, Nestle FO, Herrmann M. Additive efficacy of a bispecific anti–TNF/IL-6 nanobody compound in translational models of rheumatoid arthritis. Sci Transl Med. 2023;15(681):4419.
6. Law ST, Taylor PC. Role of biological agents in treatment of rheumatoid arthritis. Pharmacol Res. 2019;150: 104497.
7. Deng C, Zhang Q, He P, Zhou B, He K, Sun X, Lei G, Gong T, Zhang Z. Targeted apoptosis of macrophages and osteoclasts in arthritic joints is effective against advanced inflammatory arthritis. Nat Commun. 2021;12(1):2174.
8. Kurowska-Stolarska M, Alivernini S. Synovial tissue macrophages in joint homeostasis, rheumatoid arthritis and disease remission. Nat Rev Rheumatol. 2022;18(7):384–97.
9. Zhu Y, Zhao T, Liu M, Wang S, Liu S, Yang Y, Yang Y, Nan Y, Huang Q, Ai K. Rheumatoid arthritis microenvironment insights into treatment effect of nanomaterials. Nano Today. 2022;42: 101358.
10. Alivernini S, MacDonald L, Elmesmari A, Finlay S, Tolusso B, Gigante MR, Petricca L, Di Mario C, Bui L, Perniola S, Attar M, Gessi M, Fedele AL, Chilaka S, Somma D, Sansom SN, Filer A, McSharry C, Millar NL, Kirschner K, Nerviani A, Lewis MJ, Pitzalis C, Clark AR, Ferraccioli G, Udalova I, Buckley CD, Gremese E, McInnes IB, Otto TD, Kurowska-Stolarska M. Distinct synovial tissue macrophage subsets regulate inflammation and remission in rheumatoid arthritis. Nat Med. 2020;26(8):1295–306.
11. Murray PJ. Macrophage polarization. Annu Rev Physiol. 2017;79(1):541–66.
12. Zhang M, Zhang R, Dong Y, Liu J, Gao Z, Zhou X, Cao J. Oxygen supplementation liposomes for rheumatoid arthritis treatment via synergistic phototherapy and repolarization of M1-to-M2 macrophages. Chem Eng J. 2023;459: 141484.
13. Kalashnikova I, Chung S-J, Nafiujjaman M, Hill ML, Siziba ME, Contag CH, Kim T. Ceria-based nanotheranostic agent for rheumatoid arthritis. Theranostics. 2020;10(26):11863–80.
14. Kim J, Kim HY, Song SY, Go S-H, Sohn HS, Baik S, Soh M, Kim K, Kim D, Kim H-C, Lee N, Kim B-S, Hyeon T. Synergistic oxygen generation and reactive oxygen species scavenging by manganese ferrite/ceria co-decorated nanoparticles for rheumatoid arthritis treatment. ACS Nano. 2019;13(3):3206–17.
15. Yang B, Yao H, Yang J, Chen C, Shi J. Construction of a two-dimensional artificial antioxidase for nanocatalytic rheumatoid arthritis treatment. Nat Commun. 2022;13(1):1988.
16. Shi J, Li J, Xu Z, Chen L, Luo R, Zhang C, Gao F, Zhang J, Fu C. Celastrol: a review of useful strategies overcoming its limitation in anticancer application. Front Pharmacol. 2020;11: 558741.
17. Lin S, Wang D, Xu C, Zhang P, Gao K, Liu C, Mei X. Therapy of rheumatoid arthritis by reactive oxygen species-responsive celastrol-loaded nanomedicines via targeting macrophages apoptosis. Mater Des. 2022;224: 111298.

18. Zhou M, Liao J, Lai W, Xu R, Liu W, Xie D, Wang F, Zhang Z, Huang J, Zhang R, Li G. A celastrol-based nanodrug with reduced hepatotoxicity for primary and metastatic cancer treatment. EBioMedicine. 2023;94:1.
19. Wu M, Chen W, Yu X, Ding D, Zhang W, Hua H, Xu M, Meng X, Zhang X, Zhang Y, Zhang A, Jia Z, Huang S, Celastrol aggravates LPS-induced inflammation and injuries of liver and kidney in mice. (1943–8141 (Print)).
20. Keast VJ. Corrosion processes of silver nanoparticles. Appl Nanosci. 2022;12(6):1859–68.
21. Neal CJ, Fox CR, Sakthivel TS, Kumar U, Fu Y, Drake C, Parks GD, Seal S. Metal-mediated nanoscale cerium oxide inactivates human coronavirus and rhinovirus by surface disruption. ACS Nano. 2021;15(9):14544–56.
22. Soh M, Kang DW, Jeong HG, Kim D, Kim DY, Yang W, Song C, Baik S, Choi IY, Ki SK. Ceria-Zirconia nanoparticles as an enhanced multi-antioxidant for sepsis treatment. Angew Chem. 2017;129(38):11557–61.
23. Zeng F, Wu Y, Li X, Ge X, Guo Q, Lou X, Cao Z, Hu B, Long NJ, Mao Y, Li C. Custom-made ceria nanoparticles show a neuroprotective effect by modulating phenotypic polarization of the microglia. Angew Chem Int Ed Engl. 2018;57(20):5808–12.
24. Zeng F, Shi Y, Wu C, Liang J, Zhong Q, Briley K, Xu B, Huang Y, Long M, Wang C, Chen J, Tang Y, Li X, Jiang M, Wang L, Xu Q, Yang L, Chen P, Duan S, Xie J, Li C, Wu Y. A drug-free nanozyme for mitigating oxidative stress and inflammatory bowel disease. J Nanobiotechnol. 2022;20(1):107.
25. Dubertret B, Skourides P, Norris DJ, Noireaux V, Brivanlou AH, Libchaber A. In vivo imaging of quantum dots encapsulated in phospholipid micelles. Science. 2002;298(5599):1759–62.
26. Rivera-Gil P, Jimenez De Aberasturi D, Wulf V, Pelaz B, Del Pino P, Zhao Y, De La Fuente JM, Ruiz De Larramendi I, Rojo T, Liang X-J. The challenge to relate the physicochemical properties of colloidal nanoparticles to their cytotoxicity. Acc Chem Res. 2013;46(3):743–9.
27. Bao Q, Hu P, Xu Y, Cheng T, Wei C, Pan L, Shi J. Simultaneous blood–brain barrier crossing and protection for stroke treatment based on edaravone-loaded ceria nanoparticles. ACS Nano. 2018;12(7):6794–805.
28. Jiang N, Hu J, Li J, Shang K, Lu N, Wu Y. Plasma-catalytic degradation of benzene over Ag–Ce bimetallic oxide catalysts using hybrid surface/packed-bed discharge plasmas. Appl Catal B. 2016;184:355–63.
29. Murugadoss G, Kumar DD, Kumar MR, Venkatesh N, Sakthivel P. Silver decorated CeO2 nanoparticles for rapid photocatalytic degradation of textile rose bengal dye. Sci Rep. 2021;11(1):1080.
30. Parashar PK, Komarala VK. Engineered optical properties of silver-aluminum alloy nanoparticles embedded in SiON matrix for maximizing light confinement in plasmonic silicon solar cells. Sci Rep. 2017;7(1):12520.
31. Prieto P, Nistor V, Nouneh K, Oyama M, Abd-Lefdil M, Díaz R. XPS study of silver, nickel and bimetallic silver–nickel nanoparticles prepared by seed-mediated growth. Appl Surf Sci. 2012;258(22):8807–13.
32. Roubenoff R, Freeman LM, Smith DE, Abad LW, Dinarello CA, Kehayias JJ. Adjuvant arthritis as a model of inflammatory cachexia. Arthritis Rheum. 1997;40(3):534–9.
33. Li C, Li H, Wang Q, Zhou M, Li M, Gong T, Zhang Z, Sun X. pH-sensitive polymeric micelles for targeted delivery to inflamed joints. J Control Release. 2017;246:133–41.
34. Lee A, Choi S-J, Park K, Park JW, Kim K, Choi K, Yoon S-Y, Youn I. Detection of active matrix metalloproteinase-3 in serum and fibroblast-like synoviocytes of collagen-induced arthritis mice. Bioconjug Chem. 2013;24(6):1068–74.
35. Ge P, Niu B, Wu Y, Xu W, Li M, Sun H, Zhou H, Zhang X, Xie J. Enhanced cancer therapy of celastrol in vitro and in vivo by smart dendrimers delivery with specificity and biosafety. Chem Eng J. 2020;383: 123228.
36. Han Z, Gao X, Wang Y, Cheng S, Zhong X, Xu Y, Zhou X, Zhang Z, Liu Z, Cheng L. Ultrasmall iron-quercetin metal natural product nanocomplex with antioxidant and macrophage regulation in rheumatoid arthritis. Acta Pharm Sinica B. 2023;13(4):1726–39.
37. Li J, Hao J. Treatment of neurodegenerative diseases with bioactive components of Tripterygium wilfordii. Am J Chin Med. 2019;47(04):769–85.
38. Cascão R, Fonseca JE, Moita LF. Celastrol: a spectrum of treatment opportunities in chronic diseases. Front Med. 2017;4:69.
39. Yu H, Jin F, Liu D, Shu G, Wang X, Qi J, Sun M, Yang P, Jiang S, Ying X. ROS-responsive nano-drug delivery system combining mitochondria-targeting ceria nanoparticles with atorvastatin for acute kidney injury. Theranostics. 2020;10(5):2342.
40. Wang B, Shen J, Wang X, Hou R. Biomimetic nanoparticles for effective Celastrol delivery to targeted treatment of rheumatoid arthritis through the ROS-NF-κB inflammasome axis. Int Immunopharmacol. 2024;131: 111822.
41. Zhang W, Huang Y, Li J, Zhou M, Huang W, Sun L, Gui S, Li Z. Carrier-free poly (glycyrrhetinic acid)-facilitated celastrol-loaded nanoparticle for high-efficiency low-toxicity treatment of rheumatoid arthritis. Mater Des. 2024;241: 112951.
42. Rao K, Roome T, Aziz S, Razzak A, Abbas G, Imran M, Jabri T, Gul J, Hussain M, Sikandar B. Bergenin loaded gum xanthan stabilized silver nanoparticles suppress synovial inflammation through modulation of the immune response and oxidative stress in adjuvant induced arthritic rats. J Mater Chem B. 2018;6(27):4486–501.
43. Veronesi G, Aude-Garcia C, Kieffer I, Gallon T, Delangle P, Herlin-Boime N, Rabilloud T, Carrière M. Exposure-dependent Ag+ release from silver nanoparticles and its complexation in AgS 2 sites in primary murine macrophages. Nanoscale. 2015;7(16):7323–30.

Publisher's Note